COBEM 2023 27TH INTERNATIONAL CONGRESS OF MECHANICAL ENGENEERING

ABCM Brazilian Society of Mechanical Sciences and Engineering
27th ABCM International Congress of Mechanical Engineering
December 04-08, 2023, Florianópolis-SC, Brazil

# COB-2023-1600
# EFFECT OF LASER POWDER BED FUSION PARAMETERS ON DENSIFICATION BEHAVIOR AND MICROHARDNESS OF INCONEL 625/NbC COMPOSITES

**Amanda da Cunha Lemos**
**Guilherme Maziero Volpato**
**Erick Cardoso Costa**
**Fábio Antônio Xavier**
**Milton Pereira**
**Márcio Celso Fredel**
Mechanical Engineering Department, Federal University of Santa Catarina, Florianópolis, Brazil
amandacllemos@gmail.com
guilhermemvolpato@gmail.com
erickcardoso.eng@gmail.com
f.xavier@ufsc.br
Milton.pereira@ufsc.br
m.fredel@ufsc.br

***Abstract.*** *Nickel-based superalloys, such as Inconel 625, are suitable materials for high-temperature aerospace applications. However, their relative high density induces creep damage in associated materials. Adding a ceramic reinforcement to a metal matrix can reduce material density and absorb part of the load suffered. Niobium carbide (NbC) is a promising reinforcement material with high strength and limited research. Laser powder bed fusion (L-PBF) is an additive manufacturing technology that can produce metal matrix composites with high density and reduced post-processing requirements. Previous work approaches L-PBF as a promising method for producing complex geometry components with high production rates and accuracy. However, the set of L-PBF parameters influences defect formation and density of structures, requiring a strategic combination. This study investigates the effects of L-PBF processing parameters on densification behavior and microhardness of Inconel 625 composites reinforced with (10 wt%) NbC particles. The parameters of laser power and scanning speed where variable, while the layer thickness, hatch spacing and scanning strategy were maintained the same. The results show that L-PBF is a potential route for aerospace components development, as samples with relative high density and microhardness were produced through the selection of suitable values for laser powder and scanning speed.*

***Keywords:*** *Laser powder bed fusion, metal matrix composites, microhardness, Inconel 625, densification*

## 1. INTRODUCTION

Nickel-based super alloys, such as Inconel 625, have a high strength, excellent fatigue, and creep resistance (Tian *et al*., 2019), finding major application in high temperature bearing conditions, especially when operating temperatures are over about 600˚C, which is the case of aerospace components (Reed, 2006). Inconel series alloys are suitable materials for aircraft engines and gas turbines, applied in blades and discs (Reed, 2006). However, nickel-based superalloys have a limiting operating condition due to their relative high density, which induces creep damage in associated materials (Boyce, 2002). In this instance, metallic alloy conditions may be enhanced with the addition of a ceramic reinforcement phase, resulting in a Metal Matrix Composite (MMCs).

The composites often generate materials with superior properties when compared to the non-reinforced varieties (Kainer,2006). In case of aerospace applications this characteristic is particularly important, considering ceramic particles can reduce material density and decrease creep rate by acting as a load support mechanism which receives the mechanical stresses, previously absorbed by the metallic matrix (Lemos *et al.,*2022). The MMC will them improve creep resistance by load withstand and material density reduction. Niobium carbide (NbC) is a favorable variety of reinforcement due to high melting point, high hardness, and high thermal and electrical conductivity (Cuppari and Santos, 2016), with limited research in the literature, considering the inferior niobium availability in foreign countries. However, such materials are difficult and costly to fabricate with machining or subtractive processing.

A valuable tool for production of materials with such restrictions is the additive manufacturing (AM) technology. Widely developed in the past years, AM embraces the production of components with a layer-by-layer material deposition, according to a computer-aided design (CAD) model (Volpato and Tetzlaff and Fredel, 2022). As a near net-shaped technology, AM is capable of building parts with lower requirement of post processing treatment, at high

production rates and accuracy, with lower costs (Sheshadri *et al*., 2021). When one considers components features, additive manufacturing has the ability to create complex and freedom design geometries, achieving high density products for wide applications. Laser Powder Bed Fusion (L-PBF) is a promising AM technique for metal matrix composites production, which also reduces material waste, an important accomplishment for high value materials such as nickel-based superalloys. In L-PBF systems, a high-density energy laser source is employed on the complete melting and heating of pre-laid metal powders (Tian *et al*., 2019).

L-PBF is technique in which the component is produced through a stepwise process. A powder layer is added on a substrate plate and scanned with a laser beam, which causes localized melting and rapid solidification of the powder. The scanning pattern is established by the geometry of the component, which is converted into a sliced CAD model. The program divides the building part as a sequency of cross sections with their thickness equaling the layer thickness of the L-PBF process parameter (Hitzler *et al*., 2018). After scanning a certain layer, the substrate plate is lowered by a pre-determined amount. A new powder is distributed on top of the previous layer by an inbuilt recoater system, scanned and melted with the laser beam (Hitzler *et al*., 2018). The process is repeated for the subsequent layers until the entire component is formed, with the summation of the overlapped individual layers. In the end of the last layer, loose non-molten powder is removed, and, if necessary, post-processing steps are performed. Figure 1 illustrates the L-PBF process.

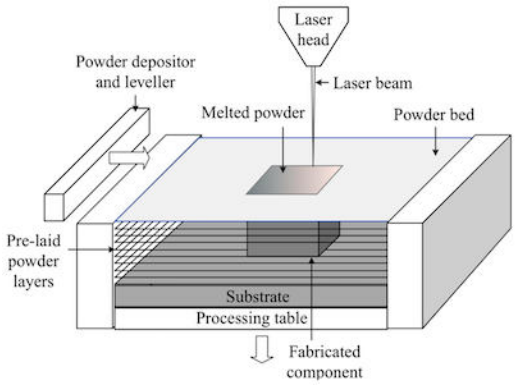


Figure 1. L-PBF process (Mumtaz and Hopkinson, 2010).

Previous studies investigated the influence of L-PBF processing parameters on the mechanical and microstructural characterization of nickel-based superalloys when varied over a certain range. Scanning speed and hatch spacing were reported as major influence factors on the porosity of the build parts (Yap *et al*., 2017). Samples with densities exceeding 99.8% were produced through the selection of optimal values for laser power and scanning speed (Benoit *et al*., 2021). According to Sheshadri *et al*. (2021), laser powder was the most contributing factor on the microhardness of samples fabricated with L-PBF, followed by the scanning speed. Thus, processing parameters need to be properly controlled to produce best quality parts with dense structures and less defects formation.

In this context, the present work investigates the effect of laser powder bed fusion processing parameters on densification behavior and microhardness of Inconel 625 composites reinforced with (10 wt%) NbC particles. Considering the area of investigation, the factors laser power and scanning speed where variable among the samples, while the layer thickness, hatch spacing and scanning strategy were maintained the same.

## 2. MATERIALS AND METHODS

In this section, details are presented regarding the powder preparation, the experimental planning, and the analyses performed.

### 2.1 Powder Characterization

To produce the composites, commercially available Inconel 625 powder was used, with a chemical composition according to Table 1 and particle size distribution with diameters between 106 and 150 μm.

Table 1. Chemical composition of Inconel 625 used in the samples.

| | Cr | Mo | Fe | Nb+Ta | Ti | Al | Si | Mn | Co | C | Ni |
|---|---|---|---|---|---|---|---|---|---|---|---|
| %wt | 22.30 | 8.50 | 2.80 | 3.50 | 0.10 | 0.10 | 0.15 | 0.10 | 1.00 | 0.03 | Bal |

Niobium carbide type 551 (NbC 551) was supplied by CBMM, according to safety information sheets CAS: 12069-94-2 and CE: 235-117-8. The mixing and homogenization of niobium carbide in a proportion of 10 wt% to Inconel 625 was obtained by 24h ball milling process (Cienlab CE-300/120) at CERMAT/UFSC.

Scanning electron microscopy (SEM) images revelated that Inconel 625 powder particles were fairly spherical (Figure 2a). In contrast, the NbC particles presented irregular shape and are agglomerated (Figure 2b). The SEM image of the mixed powder (90 wt.% IN625 and 10 wt.% NbC) (Figure 2c) shows that the NbC reinforcement covers de IN625 particles on a non-uniform way and a parcel of niobium carbide particles continued agglomerated.

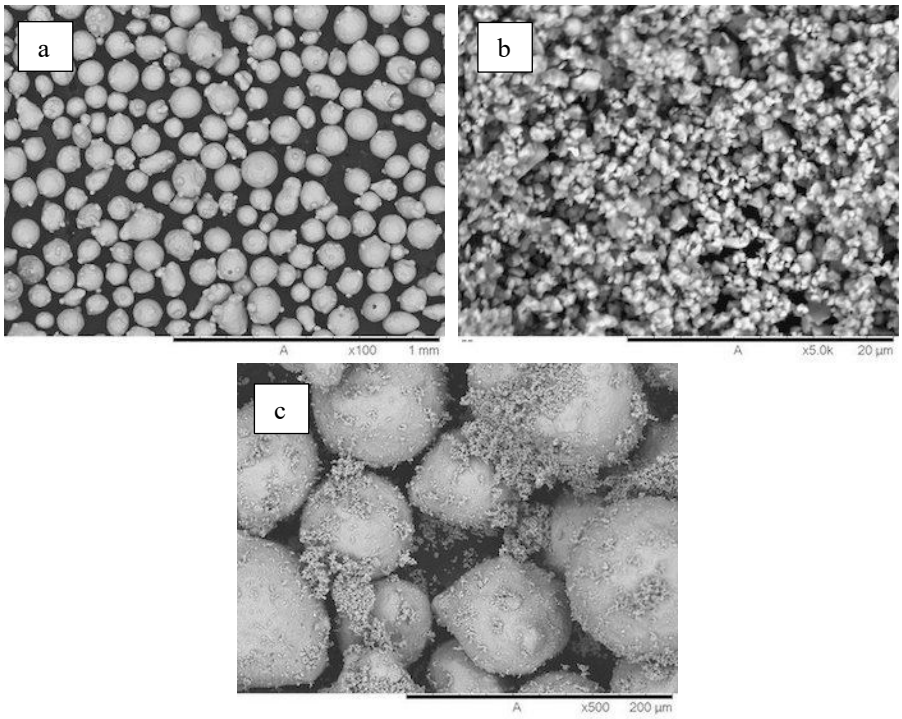


Figure 2. Scanning electron microscopy micrographs of the powders used in the process: (a) Inconel 625 powder; (b) Niobium carbide powder and IN625/NbC mixed powder (c). Backscattered contrast.

## 2.2 Laser Powder Bed Fusion process

For the manufacture of the composites, a commercial laser powder bed fusion system (Laser Funde 200, Alkimat Tecnologia Ltda, Brazil) was used. The system has a cylindrical working volume of 170 x 200 mm (diameter x height) and an inert nitrogen atmosphere. Equipped with an ytterbium doped fiber laser emitting light at a wavelength of 1064 µm, the system operates at a maximum power of 200 W and a laser spot size of 70 to 100 µm.

A total of 10 Inconel 625/NbC block samples with dimensions of 10 x 10 x 4 mm (length x width x height) were manufactured (Figure 3), varying the laser power, and scanning speed parameters according to Table 2. The layer thickness was maintained constant at 0.1 mm, just as the hatch spacing at 0.1 mm, and the laser spot size, at 0.1 mm. The scanning strategy employed was unidirectional with a rotation of 67˚ between layers. The resultant laser energy density Є was calculated with Eq. (1),

$$E\ [\mathrm{J/mm^3}] = \frac{P}{h\,.\,v\,.\,t} \tag{1}$$

where $P$ is the laser power (W), $h$ is the hatch spacing (mm), $v$ is the laser scan speed (mm/s), and $t$ is the layer thickness (mm). Laser energy density values are also displayed in Table 2.

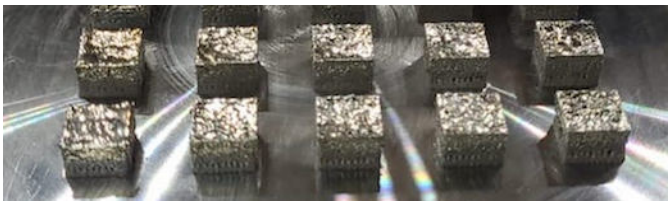

Figure 3. L-PBF produced samples.

Table 2. L-PBF process parameters of samples.

| Sample no. | Laser Power (W) | Scanning Speed (mm/s) | Laser Energy Density ($J/mm^3$) |
|---|---|---|---|
| 1 | 150 | 30 | 500 |
| 2 | 170 | 30 | 567 |
| 3 | 180 | 30 | 600 |
| 4 | 190 | 30 | 633 |
| 5 | 200 | 30 | 667 |
| 6 | 150 | 80 | 188 |
| 7 | 170 | 80 | 213 |
| 8 | 180 | 80 | 225 |
| 9 | 190 | 80 | 238 |
| 10 | 200 | 80 | 250 |

### 2.3 Densification behavior and microhardness

For density characterization, wire electrical discharge machining (EDM) was used to cut the samples across the horizontal direction, for cross-section analysis. An EDM system of model FW1U from +GF+ AgieCharmilles of Federal Institute of Santa Catarina (IFSC) with a 0.18 mm diameter molybdenum wire was used for the process. For this particular wire cut EDM machine the peak current was set at 7 A, the on-time pulse duration at 24 µm and the off-time pulse duration at 14 µs.

After the cutting process, the samples were grinded using emery paper from 80 grit size to 1200 grit size. Further, polishing was performed using a colloidal $Al_2O_3$ solution. The samples were not etched prior to imaging. Optical micrographs of the samples were obtained using a Axio Lab. A1, Carl Zeiss AG, Germany, microscope.

The analyses of density, pore area, and pore diameter were performed based on optical microscope images processed with a porosity measurement program developed in Python based on the OpenCV package.

Microhardness measurements on the L-PBF parts were carried out using a Vickers intender on a microhardness machine (SHIMADZU), according to the international standard ASTM E384-22. Indentations are taken at 3 distinct locations along each sample, subject to a load of 100 g and 15 s of dwell time. For each experimental trial, an average microhardness was calculated.

## 3. RESULTS AND DISCUSSION

Figure 4 illustrates the microscope micrographs from samples 1-10, where the areas in black represent pore area.

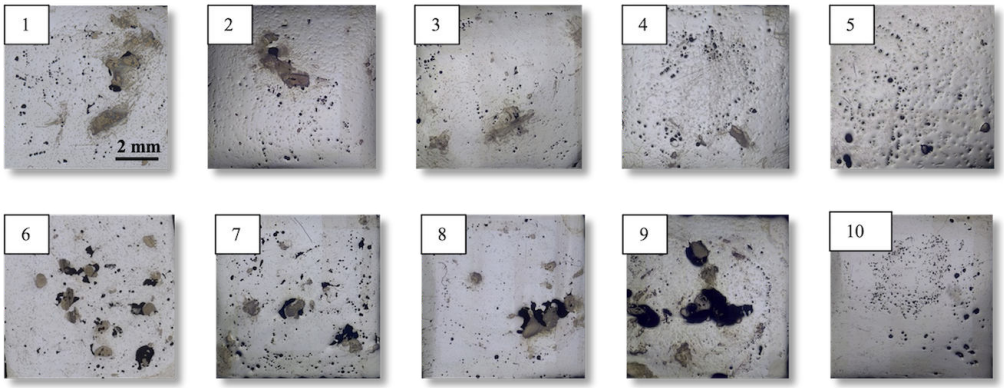


Figure 4. Micrographs of optical microscope, samples 1-10.

A qualitative analysis of Figure 4 images shows that pores are mainly from two types, namely circular and irregular shaped. Circular pores are in general formed from entrapped gases inside the melting pool, while irregular pores are normally obtained from lack of fusion powder zones, due to insufficient energy (Benoit *et al*., 2021). The process parameters laser power ($P$) and scanning speed ($v$) influence directly on the behavior of the melting pool, amount of energy available and thus, shape of pores. Considering $P$ and $v$, two scenarios are possible for each type of pores. At constant $v$, if $P$ is increased, the laser penetration is increased too, along with the depth of the melting pool, resulting in a

complete fusion of the powder. However, at higher values of *P*, vaporization effects are induced as a result of increased melting pool temperatures, which lead to entrapped gases and then circular pores. The same type of pore is observed when *P* is constant, and *v* is decreased.

At lower *v* values, a greater amount of energy is available and accumulated, due to more interaction between the laser source and the powder bed. This phenomenon also contributes to vaporization of low boiling point alloying elements and thus the formation of circular pores. At constant *v*, if *P* is decreased, less energy is available and so laser penetration is decreased. The melting pool depth is reduced and insufficient to melt the powder layer, which leads to irregular shaped pores due to lack of fusion. At constant *P*, if *v* is increased, the energy accumulation is decreased. At higher scan speed values, the laser source remains for a shorter time on the powder bed, also resulting in lack of fusion and irregular pores.

Careful analysis of Figure 4 supports the discussed theories, as samples 1-5 produced with $v$ = 30 mm/s showed mainly circular pores, while samples 6-10 produced with $v$ = 80 mm/s presented some irregular shaped pores. Laser power reveals a secondary influence when compared to scan sped for samples 1-5. On the other hand, samples from 6 ($P$ = 150 W) to 9 ($P$ = 190 W) demonstrate a clear difference on irregular pores numbers while laser power is increased. However, for this group of samples the relation is non-linear considering sample 9 showed the highest number of irregular pores off all the samples. Non-expected results can be verified in sample 10 ($P$ = 200 W), which exhibits circular pores in a greater number than other samples fabricated with similar scanning speed and lower laser power values. Table 3 exhibits the density of each sample calculated with the porosity measurement program.

Table 3. Optical density of samples.

| Sample code | 1 | 2 | 3 | 4 | 5 | 6 | 7 | 8 | 9 | 10 |
|---|---|---|---|---|---|---|---|---|---|---|
| Optical density (%) | 98.90 | 99.10 | 98.10 | 99.32 | 97.60 | 96.18 | 97.13 | 97.16 | 89.41 | 97.88 |

Dense samples with density higher than 98.5% were samples 4 (99.32%), 2 (99.10%) and 1 (98.90%), which were produced using the following parameters: 4 ($P$ = 190 W, $v$ = 30 mm/s, $E$ = 633 J/mm$^3$), 2 ($P$ = 170 W, $v$ = 30 mm/s, $E$ = 567 J/mm$^3$), 1 ($P$ = 150 W, $v$ = 30 mm/s, $E$ = 500 J/mm$^3$). All those samples produced with the same value of scan speed proved a greater influence of this process parameter on densification behavior. It is possible to assume that higher laser energy density values where required to produce high density samples, considering the greater amount of laser energy needed to melt the higher layer thickness used in this work. In Table 4, values of porosity, average pore diameter and average pore area provided from the porosity measurement program are demonstrated.

Table 4. Measurements associated with porosity, average diameter, and average area of detected pores.

| Sample | Porosity (%) | Diameter (μm) | | Area (μm$^2$) | |
|---|---|---|---|---|---|
| | | Average | Standard Deviation | Average | Standard Deviation |
| 1 | 1.10 | 32.27 | 41.27 | 2154.30 | 9181.19 |
| 2 | 0.90 | 6.77 | 13.94 | 189.79 | 3977.01 |
| 3 | 1.92 | 5.61 | 7.63 | 71.61 | 805.88 |
| 4 | 0.68 | 6.72 | 12.17 | 153.09 | 1496.42 |
| 5 | 2.40 | 7.06 | 14.10 | 196.52 | 2963.61 |
| 6 | 3.82 | 23.55 | 51.16 | 2490.80 | 25201.18 |
| 7 | 2.87 | 6.90 | 20.64 | 373.30 | 9642.97 |
| 8 | 2.85 | 9.67 | 29.85 | 774.28 | 24326.25 |
| 9 | 10.59 | 8.30 | 28.26 | 698.71 | 40904.04 |
| 10 | 2.12 | 16.87 | 26.26 | 766.22 | 4023.61 |

For this particular group of samples, the highest porosity levels were from 10.59% and 3.82% with regard to samples 9 ($v$ = 80 mm/s, $P$ = 190 W) and 6 ($v$ = 80 mm/s, $P$ = 150 W), respectively. Samples with less than 1% of porosity were produced with 30 mm/s scanning speed. As the scan speed reduces and the laser energy density increases, the porosity decreases and almost fully dense samples are obtained, with small circular pores less than 8 μm average diameter observed in the micrographs (Figure 4, samples 2-5). An analysis of the measurements in Table 4 indicates a possible influence of laser energy density on average pore diameter and average pore area. A decrease of laser energy density leads to an increase of pore size, as it is visible in Figure 4 (samples 6-10) and expected according to preferable irregular shape pores in the conditions discussed before. Samples 1 and 6 revealed higher values of diameter and pore area when compared to the tendency showed by the other samples, fabricated with similar scan speed. It appears that standard deviation is also

higher for this samples group of measurements. Samples 1 and 6 were manufactured with $P$ = 150 W, indicating that lower $P$ values induce large pore formation independent of lower scan speed.

The program also provides graphic analysis of the data information described in Table 4. An example of those results for sample 4 is shown in Figure 5.

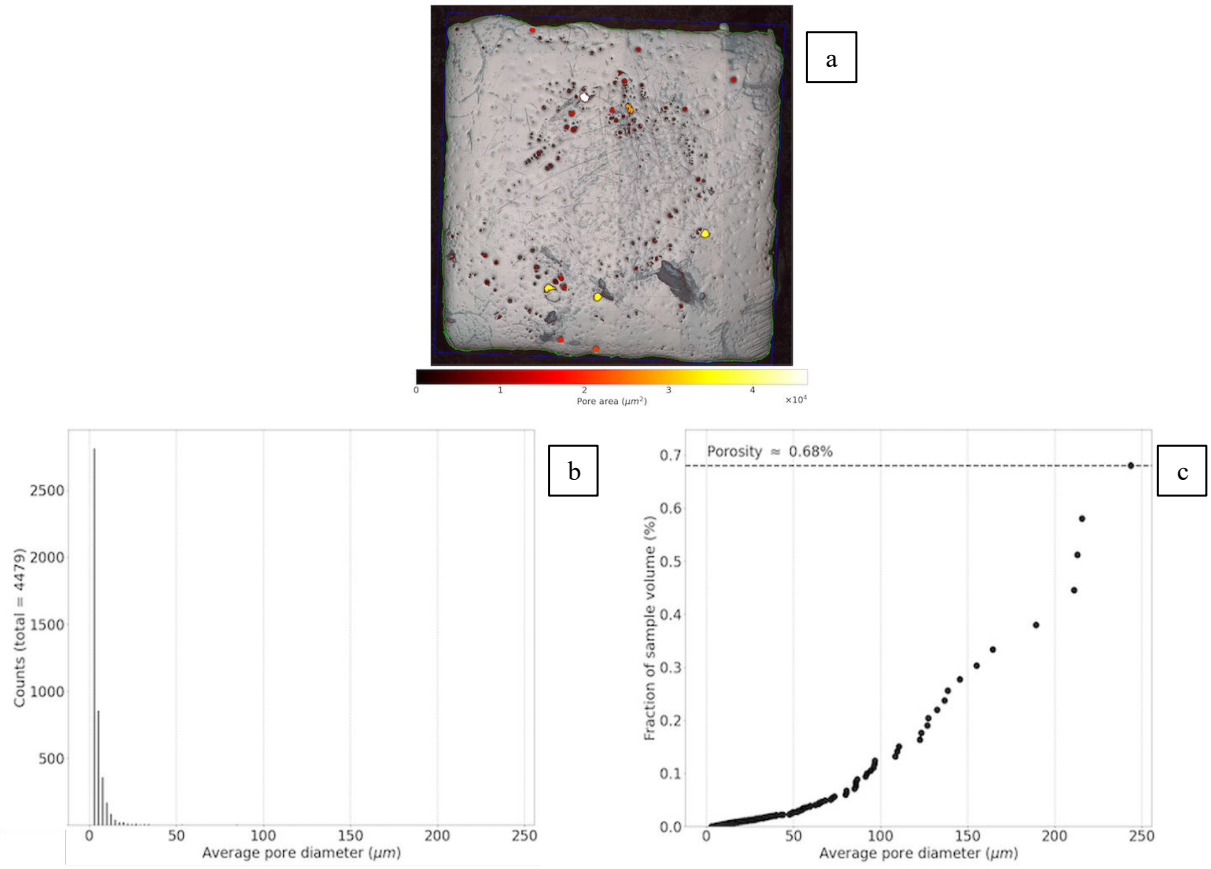


Figure 5. Graphic analysis of sample 4: (a) pore area; (b) frequency of pores; (c) accumulated porosity.

Figure 5a exhibits pore delimitation and area. Through the scale bar below the image, each shade of color defines a pore area, simplifying a visual analysis. In addition, the program gathers histograms related to the frequency of pores (Figure 5b) and accumulated porosity (Figure 5c), both related to the diameter of pores. Sample 4, represented in Figure 5, has 0.68% porosity, with frequency of pores higher up to 100 μm.

Program results of the other two higher density samples, number 2 (Figure 6) and 1 (Figure 7) are also shown. Aligned with the density results, samples 2 and 1 showed an increase in porosity of 0.90% and 1.10% respectively. The frequency of pores was also higher up to 100 μm for both samples.

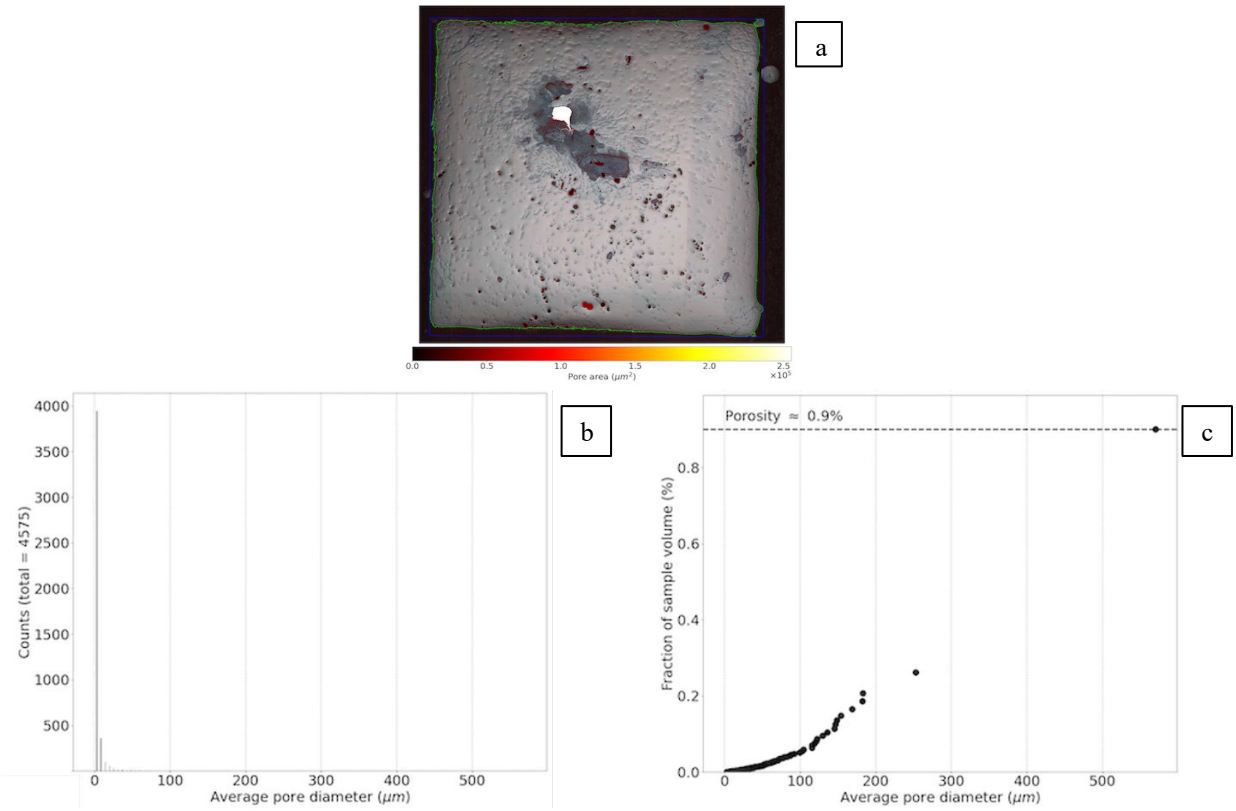


Figure 6. Graphic analysis of sample 2: (a) pore area; (b) frequency of pores; (c) accumulated porosity.

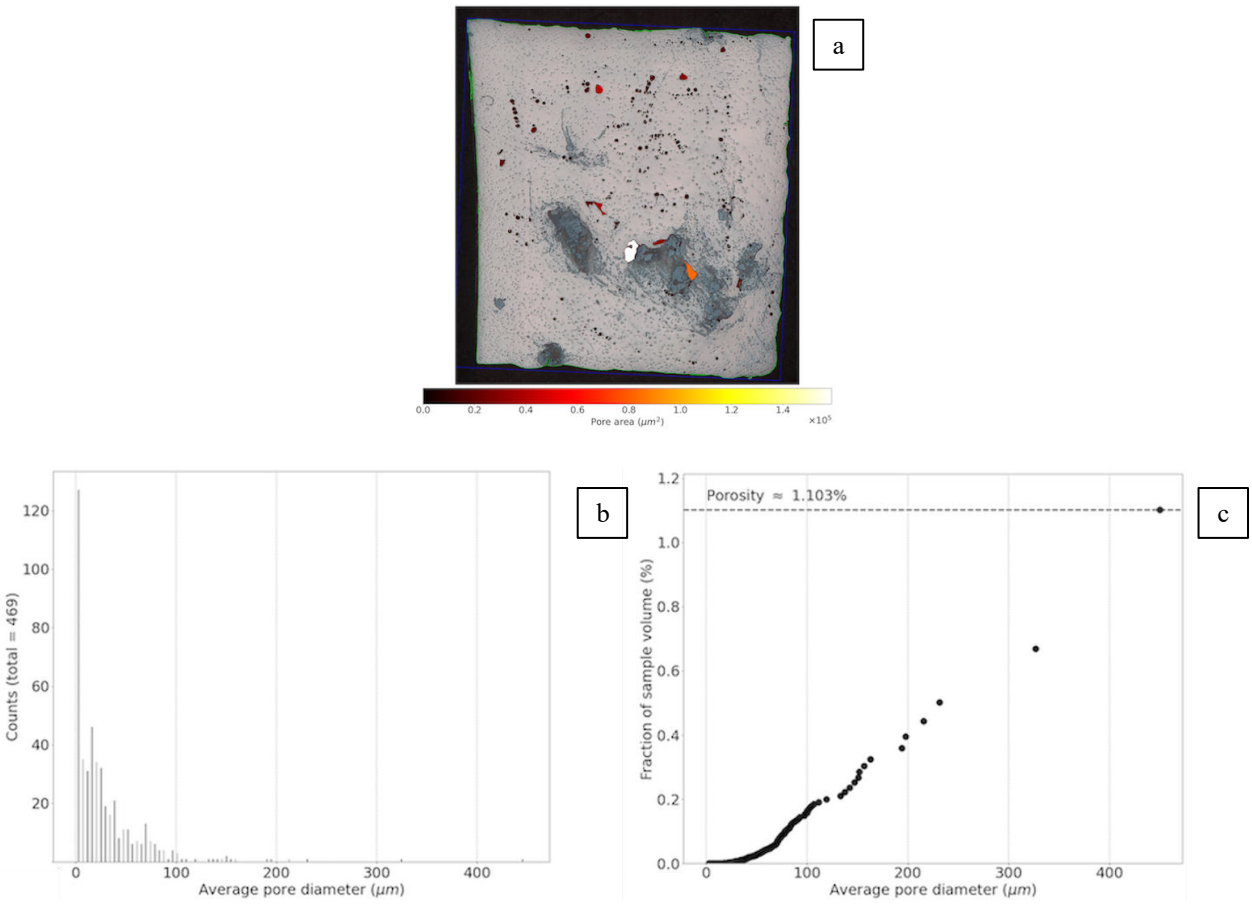


Figure 7. Graphic analysis of sample 1: (a) pore area; (b) frequency of pores; (c) accumulated porosity.

Vickers microhardness results measured along the cross section of samples 4 ($E$ = 633 J/mm$^3$), 2 ($E$ = 567 J/mm$^3$) and 1 ($E$ = 500 J/mm$^3$) are displayed on the graphic of Figure 8 in terms of laser energy density.

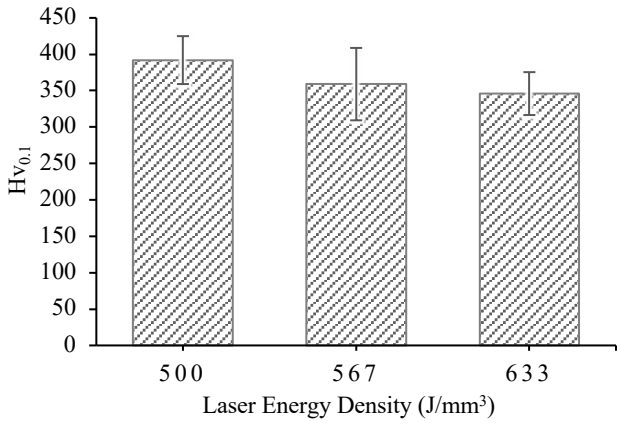


Figure 8. Average micro-hardness of L-PBF-built sample at different laser energy density.

It is observed that the average microhardness decreases with the increase in laser energy density through the decrease in laser power, considering scan speed value the same for these three samples. However, the deviation in average microhardness is minimal between samples. This occurrence can be related to the higher layer thickness used in this work, which reduces the heat dissipation and induces minimal variation in the cooling rate, at different laser energy density. Thus, the variation in grain size is not significant enough to induce microhardness variation of the samples (Nayak *et al*., 2020). A maximum microhardness value of 392 $HV_{0.1}$ was achieved by sample 1. Considering that niobium carbide tends to agglomerate, it is possible that a non-uniform distribution of those reinforcements on the matrix occurred, influencing microhardness values. Further SEM analysis are needed to confirm this hypothesis.

## 4. CONCLUSIONS

Laser powder bed fusion was successfully used to produce metal matrix composites of Inconel 625/NbC for different optimized process parameters. The samples were prepared with a varied combination of laser power and scan speed. The effects of densification behavior and microhardness of the composites were investigated. The main conclusions of the current study are as follows:

- The amount and nature of pores are dependent on the laser power and scan seed. Circular pores occurred at high laser power or lower scan speed values due to entrapped gases from vaporization in the melting pool. Irregular shaped pores were observed when laser power decreased or scan speed increased, configuring lack of fusion.
- Scan speed is seen to have the greater influence on densification behavior, considering samples with density higher then 98,5% and less than 1% of porosity were obtained at $v$ = 30 mm/s.
- The highest density achieved was 99.32%, associated with the combination of L-PBF process parameters of 190 W laser power and 633 J/mm$^3$ laser energy density.
- Average pore diameter and average pore area appear to be significantly affected by laser energy density. At higher $E$ values small circular pores, less than 8 μm average diameter, were observed.
- Higher microhardness was attributed to lower laser energy density values.

## 5. ACKNOWLEDGEMENTS

We would like to express our gratitude to Alkimat Tecnologia Ltda and the Federal Institute of Santa Catarina (IFSC) for providing access to the equipments used in this study, and the National Council for Scientific and Technological Development (CNPq) for the provided resources.

## 6. REFERENCES

Benoit, M. J., Mazur, M., Easton, M. A., and Brandt, M., 2021. “Effect of alloy composition and laser powder bed fusion parameters on the defect formation and mechanical properties of Inconel 625”. *The International Journal of Advanced Manufacturing Technology*, Vol. 114, p. 915-927.

Boyce, M. P., 2011. *Gas turbine engineering handbook*. Elsevier.

Cuppari, M. G. D. V., and Santos, S. F., 2016. “Physical properties of the NbC carbide”. *Metals*, Vol. 6, n. 10, p. 250.

Hitzler, L., Merkel, M., Hall, W., and Öchsner, A., 2018. "A review of metal fabricated with laser-and powder-bed based additive manufacturing techniques: Process, nomenclature, materials, achievable properties, and its utilization in the medical sector". *Advanced Engineering Materials*, Vol. 20, n. 5, p. 1700658.

Kainer, K. U., 2006. *Basics of metal matrix composites. Metal Matrix Composites: Custom-made Materials for Automotive and Aerospace Engineering*, p. 1-54.

Lemos, G., Fredel, M. C., Pyczak, F., and Tetzlaff, U., 2022. "Creep resistance improvement of a polycrystalline Ni-based superalloy via TiC particles reinforcement". *Materials Science and Engineering: A*, Vol. 854, p. 143821.

Mumtaz, K., and Hopkinson, N., 2010. "Selective laser melting of Inconel 625 using pulse shaping". *Rapid Prototyping Journal*, Vol. 16, n. 4, p. 248-257.

Nayak, S. K., Mishra, S. K., Jinoop, A. N., Paul, C. P., and Bindra, K. S., 2020. "Experimental studies on laser additive manufacturing of Inconel-625 structures using powder bed fusion at 100 μm layer thickness". *Journal of Materials Engineering and Performance*, Vol. 29, p. 7636-7647.

Reed, R. C., 2006. *The superalloys: fundamentals and applications*. Cambridge university press.

Sheshadri, R., Nagaraj, M., Lakshmikanthan, A., Chandrashekarappa, M. P. G., Pimenov, D. Y., Giasin, K., ... and Wojciechowski, S., 2021. "Experimental investigation of selective laser melting parameters for higher surface quality and microhardness properties: Taguchi and super ranking concept approaches". *Journal of materials research and technology*, Vol. 14, p. 2586-2600.

Tian, Z., Zhang, C., Wang, D., Liu, W., Fang, X., Wellmann, D., ... and Tian, Y., 2019. "A review on laser powder bed fusion of inconel 625 nickel-based alloy". *Applied Sciences*, Vol. 10, n.1, p. 81.

Volpato, G. M., Tetzlaff, U., & Fredel, M. C., 2022. "A comprehensive literature review on laser powder bed fusion of Inconel superalloys". *Additive Manufacturing*, Vol. 55, p. 102871.

Yap, C. Y., Tan, H. K., Du, Z., Chua, C. K., & Dong, Z., 2017. "Selective laser melting of nickel powder". *Rapid Prototyping Journal*, Vol. 23, n.4, p. 750-757.

## 7. RESPONSIBILITY NOTICE

The authors are the only responsible for the printed material included in this paper.